Editors' Suggestion

Alignment-dependent decay rate of an atomic dipole near an optical nanofiber

P. Solano,[1,*] J. A. Grover,[1] Y. Xu,[2] P. Barberis-Blostein,[1,3] J. N. Munday,[2] L. A. Orozco,[1] W. D. Phillips,[4] and S. L. Rolston[1]

[1]*Joint Quantum Institute and Department of Physics, University of Maryland, College Park, Maryland 20742, USA*

[2]*Department of Electrical and Computer Engineering and the Institute for Research in Electronics and Applied Physics, University of Maryland, College Park, Maryland 20742-3511, USA*

[3]*Instituto de Investigaciones en Matemáticas Aplicadas y en Sistemas, Universidad Nacional Autónoma de México, Ciudad Universitaria, 04510 DF, Mexico*

[4]*Joint Quantum Institute, NIST and University of Maryland, Gaithersburg, Maryland 20899, USA*

(Received 15 July 2018; published 14 January 2019)

We study the modification of the atomic spontaneous emission rate, i.e., the Purcell effect, of ^{87}Rb in the vicinity of an optical nanofiber (∼500 nm diameter). We observe enhancement and inhibition of the atomic decay rate depending on the alignment of the induced atomic dipole relative to the nanofiber. We present calculations with two different methods that qualitatively agree with some of the results; the calculations that best agree consider the atoms as simple oscillating dipoles. This is surprising since the multilevel nature of the atoms should produce a different radiation pattern, predicting different modification of the lifetime than the measured ones. This work is a step towards characterizing and controlling atomic properties near optical waveguides, fundamental tools for the development of quantum photonics.

DOI: 10.1103/PhysRevA.99.013822

I. INTRODUCTION

Neutral atoms coupled to optical waveguides is a growing field of research [1–12]. Atom-waveguide systems enable atom-light interaction for propagating light modes. This makes them promising tools for forthcoming optical technologies in the quantum regime, such as quantum switches [13–15], diodes [16,17], transistors [18], and electromagnetically induced transparency and quantum memories [19–22]. In order to further any of these applications, it is necessary to understand and control the effects of such waveguides on nearby atoms.

Two important features result from having a waveguide with a preferential optical mode: the spatial variation of the electromagnetic field, and the change of its density of modes per unit frequency. One of the key atomic properties affected by both is the spontaneous emission rate [23]. Its modification is due to the change in the local vacuum field felt by the atom under the boundary condition imposed by the adjacent object, a phenomenon known as the Purcell effect [24,25]. When the symmetry of the free-space vacuum field is broken in the presence of an object, the alignment of the atomic dipole relative to the object also plays an important role in determining the atomic lifetime. For a given alignment the atom can couple more strongly (weakly) to the vacuum modes, producing an increase (decrease) of the spontaneous emission rate. The effect of waveguides on the spontaneous emission of nearby emitters has been a productive field of research [26–38].

Optical nanofiber (ONF) waveguides [39–41] are optical fibers with a diameter smaller than the wavelength of the guided field. Most of the electromagnetic field propagates outside the dielectric body of the ONF (i.e., in vacuum) in the form of an evanescent field, and its strong transversal confinement enables interactions with adjacent atoms. The nanofiber is adiabatically connected, through a tapered section, to a conventional single-mode optical fiber, facilitating light coupling and readout. ONFs are upcoming platforms for photonic-based quantum technologies due to the coupling efficiency of light, high surface quality at the nanometer scale, and simplicity and robustness of the fabrication procedure [42]. The electromagnetic mode confinement in an ONF provides a large atom-light coupling [43,44], a feature that has been used for spectroscopy [45], atomic cloud characterizations [46,47], and atom trapping [48–53]. It also allows the operation and control of memories [19–22], and light reflectors [54,55] at the level of single photons. The presence of three polarization components of the propagating field gives rise to chiral effects and interesting possibilities for atom-light directional coupling including optical isolators [2,3,16,56].

The Purcell effect experienced by an emitter near an ONF has been studied in the past [57–66]. However, there are disagreements between predicted values for the decay rates (e.g., Refs. [58,65] differ by approximately 30% for atoms at the ONF surface), without direct experimental evidence that allows the validation of one calculation over the other. Moreover, the possibility of controlling the atomic lifetime in the vicinity of an ONF by the position and alignment of the emitter has not been emphasized or shown experimentally.

We measure the modification of the spontaneous emission decay rate of a ^{87}Rb atom near an ONF, in the time domain for different alignments of the induced atomic dipole,

*Present address: Department of Physics and Research Laboratory of Electronics, Massachusetts Institute of Technology, Cambridge, Massachusetts 02139, USA; solano.pablo.a@gmail.com

showing that the atomic lifetime can increase or decrease by the alignment of the atom. We present a theoretical description of the system, and perform both finite-difference time-domain (FDTD) and electromagnetic mode expansion calculations of the modification of the atomic decay rate. The FDTD numerical calculations considering a simple two-level atom show quantitative agreement with our experimental result. However, given the multilevel structure of the atoms, their radiation patterns should differ from that of a linear dipole. The more isotropic pattern of our multilevel atom raises a puzzling question about the interpretation of the measured effects. Nonetheless, this study offers insight about the possibility of controlling atomic properties near surfaces for photonics, quantum optics, and quantum information applications.

This paper is organized as follows: Section II explains the platform under study. The details of the experimental apparatus and the measurements procedure are in Sec. III, and the results are discussed in Sec. IV. We present numerical calculations for the atomic decay rate under the experimental conditions in Sec. V and a theoretical modeling of the system in Sec. VI. We comment on the role of the multilevel structure of real atoms in our experiment in Sec. VII. Section VIII presents a quantitative comparison of the results to numerical simulations. Finally, we discuss the implications of this result in Sec. IX, and conclude in Sec. X.

II. DESCRIPTION OF THE EXPERIMENT

We consider an ONF that only allows the propagation of the fundamental mode HE_{11}. Excited atoms that are close to the nanofiber can spontaneously emit not only into free space, but also into the ONF mode, as sketched in Fig. 1(a). Our goal is to measure the modified spontaneous emission rate γ of an atom placed near it, compared to the free-space decay rate γ_0. γ is the sum of the spontaneous emission rate of photons radiated into free space (in the presence of the ONF) and into

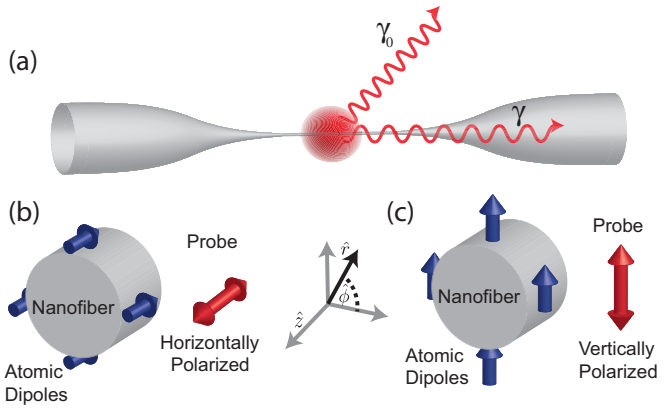

FIG. 1. (a) Sketch of the experimental configuration where a dilute ensemble of cold atoms spontaneously emit photons at a rate γ_0 or γ when they are placed far away or close to the fiber, respectively. (b), (c) Sketch of the orientation of the induced atomic dipoles relative to the nanofiber for horizontal and vertical probe beam polarization, respectively. A coordinate system considering the z axis along the ONF is used throughout the paper.

the ONF waveguide, i.e., $\gamma(\mathbf{r}) = \gamma_{\rm fs}(\mathbf{r}) + \gamma_{\rm wg}(\mathbf{r})$, where all the quantities are a function of the atom position $\mathbf{r}$. When the atom is placed far away from the ONF, $\gamma_{\rm wg} \to 0$ and $\gamma \to \gamma_0$, recovering the free-space scenario.

The atomic decay rate can be calculated from Fermi's golden rule [23,67]. It states that the decay rate from an initial state $|i\rangle$ to a final state $|f\rangle$ is given by the strength of the interaction that mediates the transition, related to $H_{\rm int}$, $(\mathbf{r})$ and the density of final states per unit energy ρ as

$$\gamma_{i\to f}(\mathbf{r}) = \frac{2\pi}{\hbar}\rho|\langle f|H_{\rm int}(\mathbf{r})|i\rangle|^2, \tag{1}$$

where $\hbar$ is the reduced Planck constant. For an electric dipole transition $H_{\rm int}(\mathbf{r}) = \boldsymbol{d}\cdot\boldsymbol{E}(\mathbf{r})$, given by the transition dipole moment $\boldsymbol{d}$ and the electric field operator $\boldsymbol{E}(\mathbf{r})$.

The electric field at the position of the atom, $\boldsymbol{E}(\mathbf{r})$, determines the atomic decay rate, given the boundary conditions [68]. In our case, the dielectric body of the ONF sets the boundary conditions, not only for the electric field propagating through the nanofiber, but everywhere near it. This changes the specific value of the atom-light coupling $|\langle f|H_{\rm int}(\mathbf{r})|i\rangle|$ along with the atomic decay rate. The dot product between the atomic dipole moment and the electric field in Eq. (1) depends upon their relative alignments, leading to alignment dependence of the atomic decay rate, because the ONF breaks the isotropy of the free-space field.

A linearly polarized optical field will induce a dipole moment in the atom along the direction of light polarization. After a scattering event, the light will leave the atom with the polarization and radiation pattern of a classical dipole aligned in that direction. By choosing the direction of light polarization we can align the radiating dipole relative to the ONF [see Figs. 1(b) and 1(c)]. This allows us to observe the dependence of the atomic decay rate on the dipole orientation. Due to the tight transverse confinement of the light propagating through the ONF, the electric field has a significant vector component along the propagation axis, as well as perpendicular to it [58]. This enables an atomic dipole oscillating along the ONF to couple light into the guided mode. This is not the case for radiation in free space, where there is no radiated power along the dipole axis [69].

Modifications in the spontaneous emission rate change the atomic spectral width and can be measured in frequency space by doing precision spectroscopy [70]. However, the atomic spectrum is highly susceptible to broadening mechanisms such as Stark, Zeeman (dc and ac), and Doppler shifts, and van der Waals effects from the ONF dielectric surface. These broadenings increase systematic errors, making the measurement more challenging. Considering this, we perform a direct atomic lifetime measurement, i.e., in the time domain, to study the atomic decay rates.

Atoms have to be relatively close to the ONF surface (less than $\lambda/2\pi$) when we probe them to see a significant Purcell effect. Two-color dipole traps, created by the evanescent field of an ONF, are a useful tool for trapping a large number of atoms close to the nanofiber [49–55]. However, the created potential minimum is usually too far from the ONF surface (typically ~200 nm) to observe changes in the atomic radiative lifetime. Cold atoms that are free to move can get much

closer to the ONF and spend sufficient time around it to be properly measured.

To measure γ/γ_0 we overlap a dilute, cold cloud of atoms with a single-mode ONF [see Fig. 1(a)]. The atoms in the cloud are excited by a resonant probe pulse propagating perpendicularly to the nanofiber. After the pulse is suddenly turned off, spontaneously emitted light is collected and the photon-triggered signals are counted and histogrammed to get their temporal distribution, a technique known as time-correlated single-photon counting (TCSPC) [71]. From the exponential decay of the temporal distribution of photons we measure the atomic lifetime $\tau = 1/\gamma$, directly related to the spontaneous emission rate. By detecting the spontaneously emitted light coupled into the ONF mode we are measuring only those atoms that are close enough to the nanofiber to couple light in. This allows us to obtain the modified spontaneous emission rate of atoms near the ONF surface. Note that the measured decay is the total decay rate γ, regardless of the mode used for the detection. The decay rates into different channels, in our case $\gamma_{\rm fs}$ and $\gamma_{\rm wg}$, only determine the branching ratio of the total decay.

We are interested in the effect of the atomic dipole alignment relative to the ONF. For this we externally drive the atomic dipole in a particular direction set by the polarization of the probe pulse. That polarization can be set to be linear in the direction along the ONF (horizontally polarized) or perpendicular to it (vertically polarized). When probing with horizontally polarized light, the atomic dipoles for two-level atoms are oriented along $\hat{z}$ [see Fig. 1(b)]. For the case of a vertically polarized probe, the atomic dipoles are oriented along $\hat{r}$ on top and bottom, but along $\hat{\phi}$ on each side, relative to the direction of propagation of the probe. In the vertical polarization case, we have a continuous distribution of dipole alignments, from dipoles along $\hat{r}$ to dipoles along $\hat{\phi}$ [see Fig. 1(c)].

III. APPARATUS AND MEASUREMENTS PROCEDURE

Figure 2(a) shows a schematic of the experimental apparatus. The ONF waist is 7 mm in length with a 240 ± 20 nm[1] radius, where the uncertainty represents the variation in any given fabrication of an ONF, as destructively measured by a scanning electron microscope and independently confirmed with nondestructive techniques [72]. We placed the ONF inside an ultrahigh vacuum (UHV) chamber. Inside the chamber, the ONF is overlapped with a cloud of cold ^{87}Rb atoms created from a magneto-optical trap (MOT), loaded from a background gas of atoms released from a dispenser. The atoms are excited by pulses of a probe beam incident perpendicularly to the nanofiber and retroreflected to reduce photon-to-atom momentum transfer. The distance from the MOT to the retroreflecting mirror is approximately half a meter, producing a temporal delay of the reflected pulse of 1.5 ns, much smaller than any other timescale involved in the experiment. These pulses are resonant with the $F = 2 \rightarrow F' = 3$ transition of

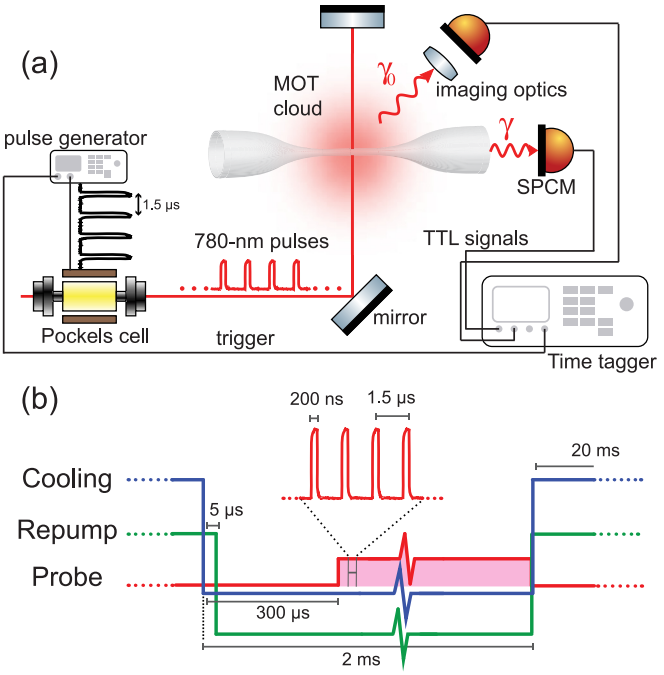

FIG. 2. (a) Schematic of the experimental setup. A train of pulses generated from a Pockels cell is directed to an ensemble of cold ^{87}Rb atoms placed near an optical nanofiber. The spontaneously emitted photons into the nanofiber are collected and time tagged to obtain the atomic radiative lifetime. Photons emitted into free space are also measured to verify possible systematic errors. (b) Experimental sequence of light pulses to cool, repump, and probe the atoms.

the D2 line and created with a Pockels cell (Conoptics 250-160) for a fast turnoff, with a pulse extinction ratio of 1:170 in 20 ns. The on-off stage of the pulses is controlled with an electronic pulse generator (Stanford Research Systems DG645). The collimated probe beam is 100 μW in power and has a $1/e^2$ width of 7 mm, kept at a saturation parameter $s < 0.05$ to reduce atomic excitations during the off period [where $s = I/I_{\rm sat} = 2(\Omega/\gamma_0)^2$, with $I_{\rm sat} = 3.58$ mW cm^{-2}, the average saturation intensity for a uniform sublevel population distribution over all m_F in $F = 2$, and Ω is the on-resonance excitation Rabi frequency]. A linear polarizer with extinction ratio of $10^5 : 1$ sets the probe polarization for driving the atomic dipoles along a particular direction. Any atoms in the cloud, close or far from the ONF, can be excited. The focusing effects of the nanofiber acting as a cylindrical lens do not affect the optical pumping or the excitation significantly according to modeling of the optical propagation. The photons emitted into the nanofiber and those emitted into free space are independently collected with avalanche photodiodes (APDs, Laser Components COUNT-250C-FC, originally specified to have less than 250 dark counts per second). The TTL pulses created from photons detected by the APDs are processed with a PC time-stamp card (Becker and Hickl DPC-230) [73] and time stamped relative to a trigger signal coming from the pulse generator. We detect of the order of 10^{-3} photons per probe pulse, consistent with considering atomic excitation probability, coupling into the ONF, power losses through band-pass filters and other optical elements, and detection efficiencies.

[1]Unless otherwise noted, all uncertainties represent one standard deviation, combined statistical and systematic uncertainty.

The experimental cycle is described in Fig. 2(b). Acousto-optic modulators (AOMs) control the amplitude and frequencies of the MOT and repump beams. After the atomic cloud reaches steady state, the MOT cooling and repump beams are turned off with a fall time of less than 0.5 μs. The repump turns off 5 μs after the cooling beams to end with the maximum number of atoms in the $F = 2$ ground state. We wait 300 μs until the AOMs reach maximum extinction. The atomic cloud constitutes a cold thermal gas around the ONF. An atom that interacts significantly with the nanofiber mode does so for approximately 1.5 μs (see atomic transit measurements in [46]). Because the atomic cloud expansion reduces the density of atoms, we limit the probing time to 1.7 ms. During this time we send a train of 200-ns probe pulses every 1.5 μs (approximately 1100 pulses). The probe beam is then turned off and the MOT beams on. We reload the MOT for 20 ms and repeat the cycle. Because the total number of atoms recaptured by the MOT beams slowly decreases over time, we restart the whole sequence after 100 cycles and reload the MOT from background pressure for about 1 s, including the computer overhead, meaning that we are taking data only $\frac{2}{3}$ of the time. The average acquisition time for an experimental realization is around 5 h, for a total of about 6.4×10^8 probe pulses.

When atoms are around the nanofiber, they tend to adhere to it due to van der Waals attraction. After a few seconds of exposing the ONF to rubidium atoms, it becomes coated with rubidium and light cannot propagate through. In order to prevent this, we use approximately 500 μW of 750-nm laser light (Coherent Ti:sapphire 899) during the MOT-on stage of the experimental cycle to create a repulsive potential that keeps the atoms away from the nanofiber surface. When the MOT beams turn off so does this "blue" beam, allowing the probed atoms to get closer to the ONF. We have also seen that 500 μW of 750-nm light is intense enough to heat the nanofiber and accelerate atomic desorption from the surface [74].

Regarding the reduction of systematic errors, all the components of the magnetic field at the position of the MOT are carefully minimized. Using three sets of Helmoltz coils we reduce all residual field components to the level of 10 mG. This reduces low-frequency quantum beats among different Zeeman sublevels (with different m_F) that will affect the apparent lifetime, and effects of atomic precession during the decay, i.e., the Hanle effect. The intensity of the probe pulse is kept much lower than the saturation intensity, in order to reduce the atomic excitation when the pulse is nominally off. Another possible systematic error is the lengthening of the measured lifetime due to radiation trapping, which is the multiple scattering of a photon between different atoms [75]. Light trapped in the sample can reexcite atoms near the ONF, creating the appearance of a longer atomic lifetime. We confirm that the atomic density is low enough by measuring the lifetime of atoms emitting into free space as a control measurement, similar to the approach followed in [76]. The photons collected from emission into free space come mainly from atoms far away from the ONF surface, so their time distribution should give us the well-known atomic lifetime $\tau_0 = 26.24(4)$ ns [77]. We also consider the modification of the probe polarization after being scattered by the nanofiber. However, given the symmetry of the problem, a horizontally polarized incoming beam does not change polarization after interacting with the ONF. On the other hand, vertically polarized light changes polarization in the transversal plane of the nanofiber. This leads to a different arrangement of dipoles aligned along $\hat{r}$ and $\hat{\phi}$ compared to a probe beam propagating unaltered, but does not change the overall distribution of dipoles aligned along both directions (see Fig. 1 for reference to the orientations).

IV. LIFETIME MEASUREMENTS

We show the normalized time distribution of photons collected through the ONF mode in Fig. 3. Figure 3(a) corresponds to a vertically polarized probe (red circles), 3(b) is free space (green diamonds), and 3(c) corresponds to a horizontally polarized probe (blue squares). The three plots show the results with the probe turned off at the same place. The inset on this figure shows the no-atom turnoff. In all three figures the background was obtained from late-time data and subtracted, and the error bars come from the statistical scatter of the data collection assuming Poissonian statistics.

Table I shows the signal-to-background noise ratio for each plot in Fig. 3, which guarantees the statistical significance of the data. We list the maximum number of counts per time bin, corresponding to the first 1.5-ns bin, and the number of background counts per time bin, which corresponds to an average over data at long times. By subtracting the background to the maximum value we extract the size of the signal, in counts per time bin, and the signal-to-background noise ratio. The data set [Fig. 3(b)] has a better signal-to-noise ratio due to two factors: a lower intrinsic dark count on the detector and more atoms in the cloud coupling to free space than atoms near the ONF surface coupling to the guided mode. Due to the geometry of the problem, an atom aligned along the ONF couples less light into the guided mode than one aligned perpendicularly, leading to a lower signal-to-background noise, which explains the statistical difference between Figs. 3(a) and 3(c).

The fits of the data to an exponential decay are shown with black lines in Fig. 3, and the plots underneath show the corresponding normalized residuals. The fit is done in a linear scale to facilitate the statistical analysis, but displayed in a semilogarithmic plot in Fig. 3 for visualization. The fitting function is $Ae^{-\gamma t}$, where the amplitude A and the decay rate γ are the only fitting parameters. Although the background is subtracted from the data, it does contribute to the noise level, and amounts to the second column in Table I, obtained from the average value of the background at long times. The value obtained for this offset with the long time average is consistent with the one obtained by letting it be an extra fitting parameter, but in order to reduce the degrees of freedom of the fit we fix it to its long time average value for every data set. The errors on each data point are the squared root of the total number of counts per bin, including background.

The statistical uncertainties of the fits represent the amount that the fitting parameter γ has to be varied to change the χ^2 by plus or minus one. These are listed in Table II. All the residuals, shown at the bottom of Fig. 3, are consistent with a Gaussian distribution, with a p value greater than 0.5 in the

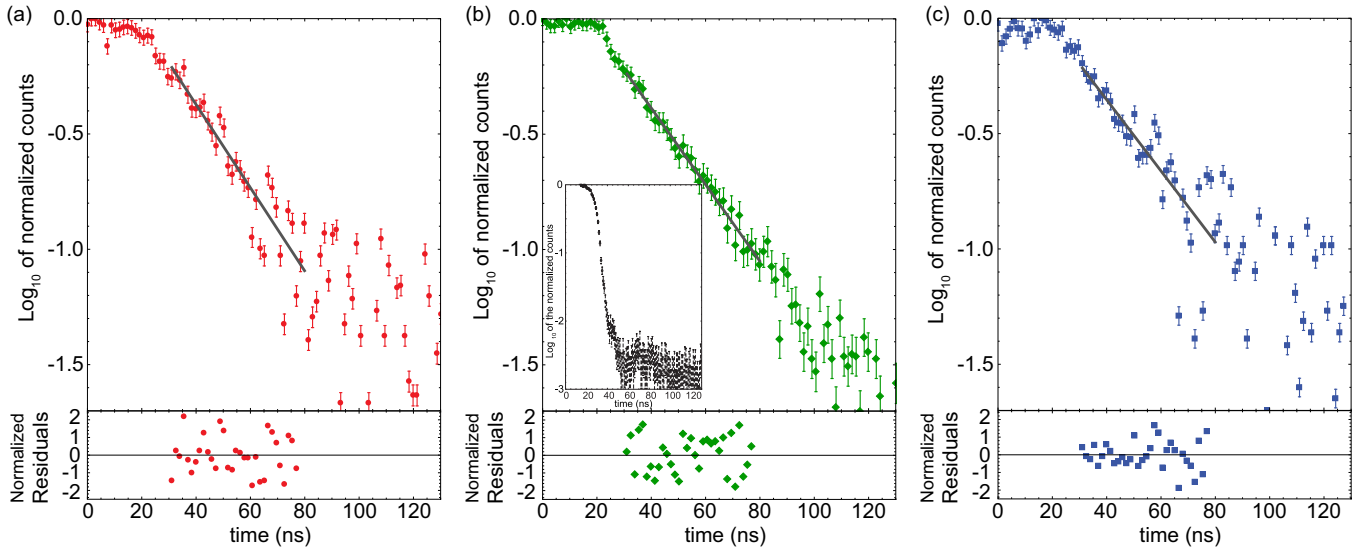

FIG. 3. Normalized time distribution of the collected photon count rate in logarithmic scale with a time bin of 1.5 ns. (a), (c) Represent the decay signal for atoms near the ONF excited with vertical and horizontal polarization, respectively. (b) Represents the decay signal for atoms in free space far from the ONF. The inset in (b) shows the excitation pulse (note the different vertical axis). The noise floor in the pulse reaches is down from the excitation by 2.5 orders of magnitude 30 ns after the pulse turns off. The black solid lines are fits to exponential decays, and their residuals normalized to the standard deviation are displayed below the plots. The fits correspond to decay rates normalized by the free-space decay rate of 1.090 ± 0.013, 1.003 ± 0.006, 0.932 ± 0.025, respectively. Each individual reduced χ^2 is 1.22, 1.14, and 0.70, respectively, with an uncertainty of ± 0.26 in all three cases. For more details of the data analysis, see the main text.

Pearson χ^2 test, and widths of 1.3 for Figs. 3(a) and 3(b), and 0.7 for 3(c).

Even though our signal to background ratio should be in principle limited by the extinction ratio of the probe pulse [better than 1:150 after one atomic lifetime, see inset in Fig. 3(b), and continuing decreasing below 1:3000], the signal is small enough that dark counts from the APDs become important and are our ultimate limiting factor. In our case, the dark counts for the detectors measuring the nanofiber channel are around 500 counts per second, a factor of 2 higher than the original specifications from the manufacturer. The free-space detector has a much lower rate. Considering our experimental duty cycle described in Sec. III, after 5 h of data we expect approximately 6.4×10^8 pulses, which means that at a rate of 500 dark counts per second we would detect 322 counts/ns only coming from dark counts, which is of the same order as column 2 in Table I.

The region of the data to fit has to be carefully chosen since the first data points of the decay can be contaminated by the turnoff signal of the probe and the last data points are dominated by background counts. This choice is a source of systematic errors. We vary the starting and ending points of the fitting curves and verify that as long as we are in a region within one to three natural lifetimes after the pulse turns off, there is no significant dependence on the chosen data points. Varying the end points did not change the obtained decay rate significantly. To keep this systematic error under control, the decay constant obtained from the data is the averaged result of decay constants from a set of different fitting regions. The obtained reduced χ^2 for different fits to the same data have a Gaussian distribution, with a width that depends on the degrees of freedom (DOF) of the fit as $\sigma_{\chi^2} = \sqrt{2/\mathrm{DOF}}$ [78]. In our case we typically fit about 30 points with two free parameters, given a $\sigma_{\chi^2} \approx 0.3$. We then consider only the fits with reduced χ^2 between 0.7 and 1.3 as reliable fits. We analyzed a total of about 300 different fits for each data set, and after applying this selection criteria 251, 206 and 85 fits were used, for Figs. 3(a), 3(b), and 3(c), respectively.

TABLE I. Counts per time bin (cts/t.b.) for the plots in Fig. 3. Rows correspond to Figs. 3(a)–3(c) from top to bottom. Counts are accumulated in a 1.5-ns time bin for about 5 h of data taking (see text for details). Maximum (Max.), signal (Sig.), background (Back.), and signal-to-background noise (Sig./$\sqrt{\text{Back.}}$).

Units	Max. cts/t.b.	Back. cts/t.b.	Sig. cts/t.b.	Sig./$\sqrt{\text{Back.}}$ $\sqrt{\text{cts/t.b.}}$
$\langle\gamma\rangle_v$	1095	469	626	29
$\langle\gamma\rangle_0$	1406	100	1306	130
$\langle\gamma\rangle_h$	1016	613	403	16

TABLE II. Error budget for lifetime measurements.

Source	Fractional error $\langle\gamma\rangle_v/\gamma_0$	$\langle\gamma\rangle_0/\gamma_0$	$\langle\gamma\rangle_h/\gamma_0$
Statistical	± 0.014	± 0.007	± 0.022
Fit	± 0.003	± 0.001	± 0.007
Magnetic field	± 0.009	± 0.009	± 0.009
Atomic density	Operating below threshold		
Probe polarization	$< \pm 0.001$		$< \pm 0.001$
Total	0.017	0.012	0.025

The systematic error of the fit listed in Table II is calculated from the standard deviation of the result from different fitting regions.

Another systematic error can be the external magnetic field. We vary the magnetic field by ±6 mT both parallel and perpendicular to the ONF without observing a significant change on the decay rate. We estimate the error from the standard deviation of the measured free-space decay rates under these small variations of the magnetic fields (see Table II).

We also change the atomic density, and effects of radiation trapping bigger than the statistical errors appear when the density increases by a factor of 3 from what we use. Because we are working well below the threshold where radiation trapping starts being relevant, we neglect the contribution of atomic cloud density to the systematic errors.

The polarization of the probe pulse might also contribute with an error from a possible tilt of the ONF. We estimate this uncertainty of the probe polarization angle to smaller than 10 mrad, and its effect on the normalized decay rate to be smaller than 0.001% (see Table II).

The apparatus, with its detection and processing of data, is the same for all measurements; this eliminates many of the possible systematic errors for the comparison of half-lives. The systematic errors listed are those that can affect the comparison (ratio), as is the case of the fitting region, the density, the polarization, and the external magnetic field.

The obtained averaged decay rates are $\langle\gamma\rangle_v/\gamma_0 = 1.088 \pm 0.017$ and $\langle\gamma\rangle_h/\gamma_0 = 0.927 \pm 0.025$ for the atoms driven by vertical and horizontal polarized probe light, respectively. The average of two independent data sets for free space is $\langle\gamma_0\rangle/\gamma_0 = 0.989 \pm 0.012$, corresponding to atoms far away from the ONF. Independent data sets obtained under the same experimental condition give fitting values with a spread within the uncertainties, validating the estimated errors. The measured Purcell effect of the ONF is only less than 10%. However, with our current signal-to-noise ratio, we measure a difference in the modified spontaneous emission decay rate between the two probe polarizations of 5 standard deviations (of the combined uncertainties).

V. NUMERICAL SIMULATIONS FOR A TWO-LEVEL ATOM

A significant fraction of the literature about modified spontaneous emission rates considers two-level atoms, i.e., classical dipoles [79,80], and we follow that in this section. We discuss the ramifications to our multilevel atoms in a later section.

The radiative decay rate of an atom can be modified by the boundary conditions of the electromagnetic vacuum. We consider calculating this modification by two different approaches. Each is presumably equally valid and provides a different perspective and intuition of the problem [68]. In the first one, when the mode expansion of the electromagnetic field of the full space is known, the contribution of each mode to the spontaneous emission rate can be calculated using Fermi's golden rule [see Eq. (1)]. In particular, the mode expansion of the vacuum electromagnetic field for an ONF has an analytical expression [58]. A second strategy, useful when the modes are unknown or too complicated to compute analytically, is to solve the problem from classical electrodynamics. We calculate the modification of the radiated power of a classical dipole under equivalent boundary conditions, and take that to be the modification of the radiative decay rate of the atom [79]

$$\frac{\gamma}{\gamma_0} = \frac{P}{P_0}, \tag{2}$$

where γ and γ_0 are the modified and unmodified atomic decay rates, respectively, and P and P_0 are the classically calculated modified and unmodified total radiative power. The modification of the radiative spontaneous emission is explained by the effect of the electric field reflected from the boundaries to the dipole position.

The latter approach allows us to develop an intuitive picture based on the idea that a two-level atom radiates as a linear dipole oscillating along the direction of the excitation field: When the atomic dipole is aligned along $\hat{z}$ or $\hat{\phi}$, parallel to the ONF surface, the radiated light can be reflected from the front and back interfaces created by the dielectric. These multiple reflections combine at the position of the dipole affecting its emission. Because there is interference between reflections, the dipole radiation is sensitive to changes in the ONF radius. For these cases, the effect of the nanofiber can lead to enhancement or inhibition of the radiative spontaneous decay rate. On the other hand, for a dipole aligned along $\hat{r}$ we can expect little radiation reflected from the back surface of the ONF to the dipole, given the radiation pattern. For this case, the decay rate depends mainly on the distance between the atom and the ONF surface and only slightly on the nanofiber radius. An alternative viewpoint is to consider image charges. The atomic dipole induces an image dipole inside the ONF aligned in the same axis and in phase. They radiate more power than the normal atomic dipole, producing an enhancement of the decay rate for the distances we consider.

Using the second strategy, based on a classical dipole, we calculate the modification of the atomic decay rate near an optical nanofiber as a function of the ONF radius and the distance from the atom to the nanofiber surface for different atomic dipole orientations. The calculation is performed numerically with a FDTD algorithm [81]. It considers the wavelength of the emitted light, and the nanofiber index of refraction to be $\lambda = 780.241$ nm and $n = 1.453\,67$, respectively. The results of these calculations are shown in Figs. 4(a)–4(c). It shows the modification of the atomic decay rate as a function of distance to the nanofiber and radius of the nanofiber for dipoles aligned (in cylindrical coordinates) in the (a) z direction, (b) ϕ direction, and (c) r direction relative to the ONF [as sketched in Figs. 1(b) and 1(c)]. We identify these rates as γ_z, γ_ϕ, and γ_r, respectively. The values of γ/γ_0 for these three cases are normalized so they are equal to one at large atom-surface distance. The numerical accuracy of the FDTD simulations is of the order of ±1% and is predominantly limited by the finite mesh size.

The atomic decay rate of an atomic dipole aligned along $\hat{z}$ [Fig. 4(a)] is mostly inhibited close to the ONF surface compared to the free-space decay rate, and it is highly dependent on the nanofiber radius. This is also true for dipoles aligned along $\hat{\phi}$ [Fig. 4(b)]. For a dipole aligned along $\hat{r}$ [Fig. 4(c)], the decay rate is enhanced and depends mostly on

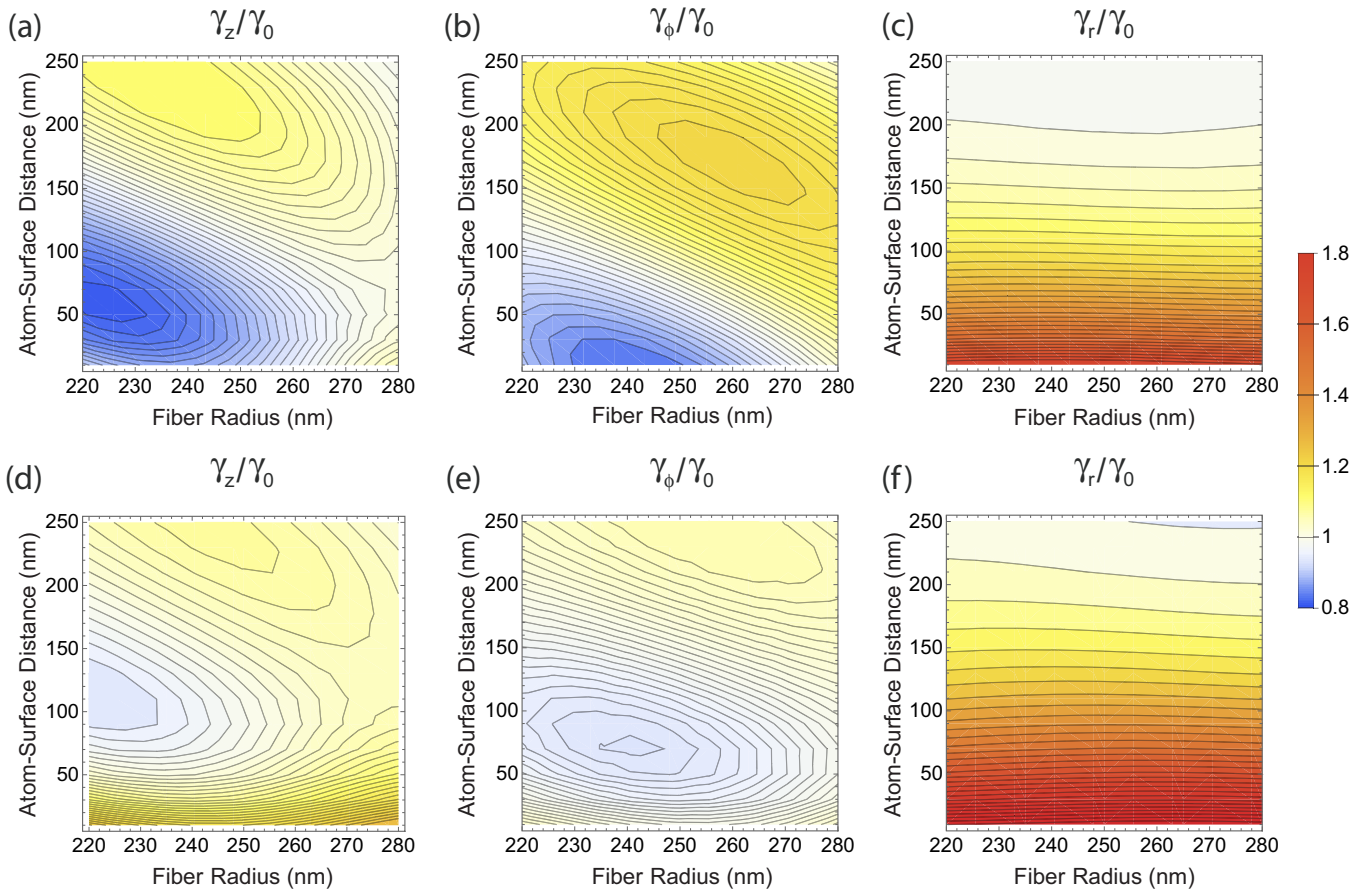

FIG. 4. Modification of the atomic spontaneous emission rate due to the presence of the ONF normalized by the free-space decay rate. The results are displayed as function of the distance between the atom and the fiber surface, and the ONF radius. The three possible atomic dipole orientations can be along $\hat{z}$, $\hat{\phi}$, and $\hat{r}$. (a)–(c) Show the result of FDTD calculation. (d), (e) Show the result of a mode expansion calculation.

the distance between the atom and the ONF surface and not on the nanofiber radius.

These results are compared with the calculations of the radiative lifetime using the electromagnetic field mode expansion (taken from Ref. [58]) in Figs. 4(d)–4(f). To corroborate the calculation, the results were compared against independent calculations based on Green functions [57,82,83]. The spread of the these different numerical calculations is below 0.1%. We are interested in the limit where only the fundamental mode of the ONF can propagate, which is valid when the ONF radius is smaller than 284 nm for a wavelength of 780 nm. We observe that both calculations are qualitatively similar, but quantitatively different. The main discrepancy occurs at the fiber surface, where the mode expansion calculation seems to give a larger enhancement of the decay rate. The reason for the disagreement between the two results is not understood. We have verified that other calculations based on finding the electric field at the position of the atom are in agreement with the mode expansion approach (compares Ref. [57,58]). On the other hand, our FDTD calculations are in agreement with previous results using the same method [65].

VI. THEORETICAL CONSIDERATIONS FOR THE MODEL

The modification of the atomic spontaneous emission is a function of the position of the atom. Because the atoms are not trapped at a particular position, the measured decay time is a spatial average of the atomic distribution around the ONF. The main factor that determines that distribution is the van der Waals interaction between the atoms and the ONF. Moreover, atoms emit into the ONF mode with different probabilities, depending on their relative orientation and proximity to the nanofiber, altering the average of the decay time.

A. Van der Waals potential

At short distances from the ONF, the atoms feel an attractive force due to the van der Waals and Casimir-Polder (vdW-CP) potentials. These two potentials can be smoothly connected in a simple equation written as [84,85]

$$U_{g,e}(r) = -\frac{C_4^{(g,e)}}{r^3\left(r + C_4^{(g,e)}/C_3^{(g,e)}\right)}, \tag{3}$$

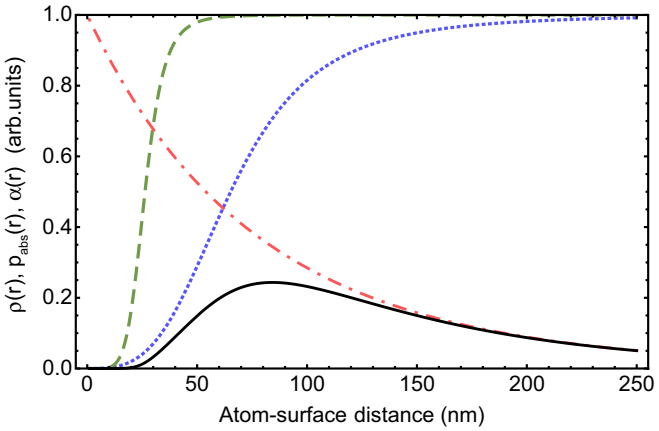

FIG. 5. Plot of the spatial dependence of $\rho(r)$ (dotted blue line), $p_{\rm abs}(r)$ (dashed green line), and $\alpha(r)$ (dotted-dashed red line) in arbitrary units as a function of the atom-surface distance. The black solid line is the direct multiplication of these functions and it represents the distribution over which the spatial average is taken in a realistic experiment, as stated in Eq. (11).

valid for the atomic ground (g) and excited (e) states, where C_3 and C_4 are the van der Waals and Casimir Polder coefficients of the atom interacting with the nanofiber. Using the procedure described in Ref. [86] we can obtain the value of these coefficients. For a ^{87}Rb atom in the $5S_{1/2}$ ground level in front of an infinite half-space fused silica medium, with index of refraction $n = 1.45$, the van der Waals and Casimir-Polder coefficients are $C_3^{(g)} = 4.94 \times 10^{-49}$ J m^3 and $C_4^{(g)} = 4.47 \times 10^{-56}$ J m^4, respectively. For the $5P_{3/2}$ excited state $C_3^{(e)} = 7.05 \times 10^{-49}$ J m^3 and $C_4^{(e)} = 12.2 \times 10^{-56}$ J m^4. The vdW-CP potential affects the experimental measurement in two different ways: by reducing the local density of atoms and by shifting the atomic levels.

By sending probe pulses to the entire atomic cloud, we actually measure a spatial average over an ensemble of atoms with a density distribution $\rho(r)$ at a radius r from the ONF surface. The vdW-CP attraction accelerates the atoms reducing the local density around the nanofiber, all of them initially in the ground state. Assuming only the radial degree of freedom and thermal equilibrium, a simple steady-state density distribution can be obtained from the ideal gas law and energy conservation [86], as

$$\rho(r) \approx \rho_0 \frac{1}{1 - U_g(r)/E}, \tag{4}$$

where ρ_0 and $E = \frac{3}{2} k_B T$ are the atomic density and the average (kinetic) energy of the atoms far away from the fiber, with atoms typically at $T \approx 150$ μK for our atomic cloud. By only considering U_g, we neglect the small fraction of atoms in the excited state. Figure 5 shows an example of this distribution (blue dotted line). This approximation agrees with previous analytical results [87], and differs at most by 30% with Monte Carlo simulations of atomic trajectories [84].

The vdW-CP potentials also shift the atomic energy levels, affecting the probability to absorb the otherwise resonant probe beam as [74]

$$p_{\rm abs}(r) = \frac{N}{1 + s + 4\left(\frac{\delta(r)}{\gamma_0}\right)^2}, \tag{5}$$

where N is just a probability normalization factor and $\delta(r) = [U_e(r) - U_g(r)]/2\pi\hbar$ is the detuning induced by the ONF, which for us is always red-shifted. This distribution is plotted with a green dashed line in Fig. 5, neglecting s since we work in the low saturation limit.

B. Coupling into the waveguide

Another factor to consider when measuring the spontaneously emitted light into the ONF is the fact that atoms that are closer to the nanofiber surface contribute more to the measured signal than those further away. This effect is characterized by the emission enhancement parameter

$$\alpha(r) = \frac{\gamma_{\rm wg}(r)}{\gamma_0}. \tag{6}$$

This factor is different from the more commonly used coupling efficiency $\beta(r) = \gamma_{\rm wg}(r)/\gamma(r)$ [39,88]. $\alpha(r)$ is proportional to the total number of photons emitted into the guided mode, and $\beta(r)$ is the percentage of photons emitted into the mode relative to the total number of emitted photons. The difference between α and β becomes clear with the following example: When the coupling efficiency $\beta(r)$ is very large, close to one, most of the emitted photons couple to the waveguide. However, the total number of photons emitted into the waveguide can still be close to zero if the total spontaneous emission were to be greatly inhibited, $\gamma \ll \gamma_0$ (which is not our particular case). The amplitude of the signal measured through the guided mode is then represented by the emission enhancement parameter $\alpha(r)$.

An analytical expression for $\gamma_{\rm wg}(r)$ can be found in the literature [58,59], and it is proportional to the norm squared of the evanescent electric field, as expressed in Eq. (1). For a single-mode ONF, the spatial dependence of each component of the evanescent electric field is given by the sum of one or two modified Bessel functions of the second kind $K_i(qr')$ of order $i = 0, 1, 2$; where $r' = r_0 + r$, and r_0 and r are the ONF radius and the radial position from the ONF surface; $q = \sqrt{\beta^2 - k^2}$ is the transverse component of the wave vector, β is the field propagation constant in the ONF, and $k = 2\pi/\lambda$ is the free-space wave number. For our particular case of an ONF with radius $r_0 = 240$ nm propagating a field of wavelength $\lambda = 780$ nm, $q = 0.59k$. Provided that $qr' > 1$ away from the ONF surface, we can simplify the calculation with the asymptotic expansion of $K_i(qr') \approx \sqrt{\pi/2qr'}e^{-qr'}$, and approximate the spatial dependence of $\gamma_{\rm wg}(r)$ as [46]

$$\alpha(r) = \frac{\gamma_{\rm wg}(r)}{\gamma_0} \propto \frac{1}{r_0 + r} e^{-2(0.59kr)}, \tag{7}$$

an approximation that has been tested against exact numerical results with excellent agreement. Any other constant prefactor will not contribute to the final average after the appropriate normalization. Its spatial distribution is plotted as the red dotted and dashed line in Fig. 5. For our experimental parameters $\alpha \approx 0.2$ at the ONF surface.

Atomic dipoles aligned along different directions will couple to the guided mode with different strengths, but with the same spatial dependence as $\alpha(r)$ in Eq. (7). We denote the emission enhancement parameter with a subindex to specify the alignment of the emitting dipole as $\alpha_i(r)$ with $i \in \{z, \phi, r\}$. It can be shown, from the calculation in Ref. [58], that to a good approximation $\alpha_z \approx \alpha_\phi \approx \alpha_r/3$ for our ONF, independent of the radial position of the atom. The different coupling strength for atomic dipoles aligned along r comes from the fact that the radial component of the guided field is discontinuous and larger than the others due to the dielectric boundary conditions.

Figure 5 shows the spatial dependence of each one of the described distributions that affect the measured average decay rate. The black solid line in the plot represents the direct multiplication of them. This effectively describes the probability of observing a photon emitted from an atom at a position r into the ONF guided mode. Notice that for a given ONF the only experimentally tunable parameter for the final distribution is the temperature of the atomic cloud. The atomic distribution is weakly dependent on the temperature in Eq. (4).

C. Averaged signal

The measured signal is an average of atoms decaying at different rates. If these decay rates are close enough to each other, the measured decay rate is approximately equal to the spatially averaged decay rate $\langle\gamma\rangle$. As a proof let us consider that the decay rates differ by a small quantity ϵ with a distribution $g(\epsilon)$, then the measured signal is given by

$$\int d\epsilon\, g(\epsilon) e^{-\gamma(1+\epsilon)t} = e^{-\gamma t} \int d\epsilon\, g(\epsilon) e^{-\gamma\epsilon t}. \tag{8}$$

For small ϵ (and short times) the exponential of order ϵ can be expanded in series, averaged, and exponentiated again, to obtain

$$e^{-\gamma(1+\langle\epsilon\rangle)t} = e^{-\langle\gamma\rangle t}. \tag{9}$$

The measured decay rate $\langle\gamma\rangle$ is a spatial average of the actual decay rate weighted by the atomic density distribution $\rho(r)$, the excitation probability $p_{\text{abs}}(r)$, and the emission enhancement parameter $\alpha(r)$:

$$\langle\gamma\rangle = \frac{\int \gamma(r)\alpha(r)\rho(r)p_{\text{abs}}(r) r\, dr}{\int \alpha(r)\rho(r)p_{\text{abs}}(r) r\, dr}. \tag{10}$$

The atomic dipole might not be completely aligned along one of the cylindrical coordinates. In this case the decay rate will be the average over the different orientations, given by

$$\langle\gamma\rangle = \sum_i \frac{\int \gamma_i(r) P_i \alpha_i(r)\rho(r)p_{\text{abs}}(r) r\, dr}{\int P_i \alpha_i(r)\rho(r)p_{\text{abs}}(r) r\, dr}, \tag{11}$$

where the index i runs through three orthogonal orientations, P_i are the probability (or projection) of having the atom in the i axis, and α_i is the emission enhancement parameter of a dipole aligned along i.

In the particular case of driving the atoms with light polarized vertically, there are atomic dipoles oriented along $\hat{r}$ and $\hat{\phi}$ [see Fig. 1(c)]. In this case the proper α_i has to be taken into account to obtain the averaged signal.

VII. CONSIDERATION OF THE MULTILEVEL ATOMIC STRUCTURE

A multilevel atom (with more than one Zeeman sub-level m_F in the ground state) is aligned when there is a symmetry axis in which the Zeeman sublevels have equal populations among states with m_F of opposite signs (see Ref. [69]). Such an axis is the direction of alignment. This contrasts with the case where the atom is in a preferential m_F, in which case we say the atom is (spin) oriented. In the absence of an external magnetic field, if we send a resonant linearly polarized beam the atom will be optically pumped to its steady state. This steady state is aligned along the polarization of the driving field, and that direction becomes a good quantization axis. This picture allows us to extend the concept of alignment from a classical dipole to a multilevel atom as a good analogy.

The radiation pattern of a real atom differs from that of an ideal linear dipole. A multilevel atom can decay to a ground state through a π or σ transition, when $\Delta m_F = 0$ or $\Delta m_F = \pm 1$, respectively. In our case, we consider the quantization axis to be along the direction of the linear polarization of the probe, and π and σ are with respect to this quantization axis. Δm_F contains all the information regarding the effect of the atomic dipole alignment, i.e., the projection of the atomic dipole moment onto the electric field vector of the nanofiber mode.

We model the decay rate of a multilevel atom by an incoherent superposition of linear dipoles [89] that describes the real radiation pattern. An atom decaying through a π transition is described by a linear dipole aligned along the probe polarization axis. An atom decaying through a σ transition is considered as a linear dipole rotating in the plane perpendicular to the probe polarization axis. The atomic decay rate depends on the norm squared of the dot product of the electric field and the dipole polarization [see Eq. (1)]. This implies that the decay rate of a rotating dipole (σ transition) is the incoherent sum of the decay rate of two orthogonal linear dipoles oscillating in the rotation plane.

All the information necessary to calculate the decay rate of different transitions of a real atom is then calculated from the decay rates of classical linear dipoles, in the spirit of Fig. 4. To calculate the total decay rate, we need to know the branching ratios of the transitions. We denote the probability of decay through a π or σ transition as P_π and P_σ, respectively, corresponding to a $\Delta m_F = 0$ and $\Delta m_F = \pm 1$ decay. These probabilities include the coupling strength of the transition, determined by the square of the Clebsch-Gordan coefficients, and the distribution of $m_{F'}$ from the initial state preparation.

The measured signal will be a spatial average over the contribution of such classical dipoles, weighted according to the coupling efficiency of each dipole into the waveguide. Considering this, the spatially averaged decay rate can be obtained using Eqs. (4), (5), and (6) as

$$\langle\gamma\rangle_\pi = \frac{\int [\gamma_\pi(r) P_\pi \alpha_\pi(r) + \gamma_\sigma(r) P_\sigma \alpha_\sigma(r)]\rho(r)p_{\text{abs}}(r) r\, dr}{\int [P_\pi \alpha_\pi(r) + P_\sigma \alpha_\sigma(r)]\rho(r)p_{\text{abs}}(r) r\, dr}, \tag{12}$$

where $\gamma_i(r)$ with $i \in \{\pi, \sigma\}$ are obtained from the numerical simulation displayed in Fig. 4. The subscript π in the spatial

average denotes the polarization of the probe beam that drives the atomic transition.

VIII. COMPARISON BETWEEN THEORY AND EXPERIMENT

We can compare the measurements with the theoretical simulations calculating the average $\langle\gamma\rangle/\gamma_0$ by introducing the numerical values of $\gamma(r)/\gamma_0$, displayed in Fig 4, into Eq. (11) for a particular ONF radius. It is important to notice that when we realize the experiment probing the atoms with horizontally polarized light, we are measuring the spatially averaged decay rate for an atomic dipole aligned along $\hat{z}$. In this case, the measured value only depends on the radial distribution of atoms. For atoms driven by a vertically polarized probe pulse we measure a decay rate that is averaged over the different dipole alignments in addition to the spatial average [along $\hat{\phi}$ and $\hat{r}$ as is shown in Fig. 1(c)]. This means that we can not separately measure the decay rate for dipoles aligned along $\hat{r}$ and $\hat{\phi}$. Assuming that the distribution of atoms is azimuthally symmetric, we can obtain the azimuthal average of the decay rate by assuming half of the atoms in the top and bottom positions (dipole aligned radially) and half of the atoms in the left and right positions (dipole aligned azimuthally), so the the final average depends only on the integral over the radial coordinate as shown in Eq. (12).

Figure 6 shows a comparison between the measurements and the numerical simulations for a two-level atom. It shows the extracted atomic decay rates for both experimental configurations normalized by the free-space one. The blue lines are the calculated value of the modified decay rate $\langle\gamma\rangle_h/\gamma_0$, corresponding to the probe beam horizontally polarized, to be compared with the experimental value (blue square). The blue dashed line corresponds to the FDTD calculation and the dotted one the mode expansion calculation. The red lines are the calculated values of the modified decay rate $\langle\gamma\rangle_v/\gamma_0$, corresponding to the probe beam vertically polarized, to be compared with the experimental value (red circle). The red dashed line corresponds to the FDTD calculation and the dotted one the mode expansion calculation. For each experimental realization, we simultaneously measure the modified atomic decay rate of atoms close to the ONF and the free-space decay rate from atoms in the MOT, where the great majority of them are away from the nanofiber. The black diamonds in Fig. 6 are the measurements of the decay rate into free space for the two different polarizations.

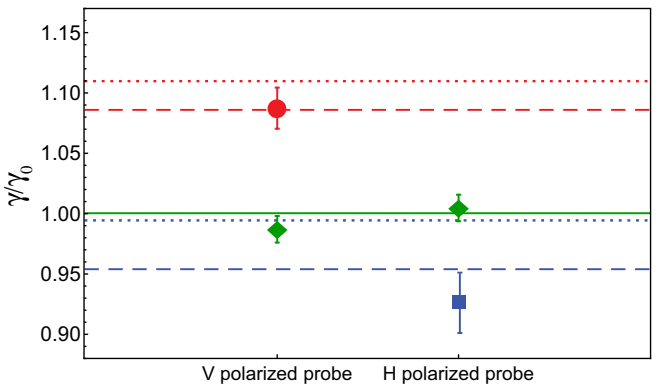

FIG. 6. Normalized decay rates for different polarizations of the probe with respect to the nanofiber. The red circle (blue square) corresponds to the measured modified lifetime of atoms driven by vertically (horizontally) polarized probe light. The green diamonds are the simultaneously measured free space decay time for each configuration. The solid green line is the expected decay rate in free space. The dashed blue and red lines are the calculated values from the two-level atom FDTD calculation for a horizontal polarized probe and a vertically polarized probe respectively. The dotted lines are the calculated values from the two-level atom mode expansion calculation. Both calculation are done considering the spatial average in Eq. (11).

For a multilevel atom, we have to consider its initial state. During the period the probe beam is on, the atoms get pumped into a particular ground state. Although the number of excitations of an atom per pulse is approximately $\frac{1}{2}$, in each experimental cycle we send over a thousand pulses to the same ensemble of atoms. After a few pulses, all the atoms have been pumped to a steady state, remaining there for the vast majority of the excitation pulses and data taking. The steady-state solution for optical pumping the $F = 2 \rightarrow F' = 3$ transition of ^{87}Rb with linearly polarized light is biased towards the $m_F = 0$ state (the fractional populations are approximately 0.04, 0.24, and 0.43 for $|m_F|$ equal 2, 1, and 0, respectively). This steady state corresponds to a multilevel atom aligned along the direction of the probe polarization [69]. A π excitation (linearly polarized) of such an initial state will lead to probability $P_\pi = 0.55$ of emitting π radiation and $P_\sigma = 0.45$ of emitting as a σ radiation (circularly polarized). This effect has to be taken into account when calculating the averaged decay rate using Eq. (12). Considering this, neither of our calculations, the FDTD nor the mode expansion, predict the measured values. We calculate values of $\langle\gamma\rangle_v^{\mathrm{FDTD}}/\gamma_0 = 1.086$ and $\langle\gamma\rangle_v^{\mathrm{mode}}/\gamma_0 = 1.110$ for a vertically polarized probe, and $\langle\gamma\rangle_h^{\mathrm{FDTD}}/\gamma_0 = 0.954$ and $\langle\gamma\rangle_h^{\mathrm{mode}}/\gamma_0 = 0.994$ for a horizontally polarized probe. Although these results are close to the measured decay rate of an atom driven with vertically polarized light, they do not predict significant inhibition of the spontaneous emission when the atom is driven with horizontal polarization.

Even if the initial population distribution is different from the calculated optical pumping values, almost all population distributions tend towards producing a more isotropic radiation pattern than a linear dipole, as any amount of sigma polarization reduces the angular contrast. For example, if we were to start in the state $m_F = 0$, then $P_\pi = \frac{3}{5}$ and $P_\sigma = \frac{2}{5}$, a fairly isotropic pattern. On the other hand, if we were to start in the state $m_F = 2$, then $P_\pi = \frac{1}{3}$ and $P_\sigma = \frac{2}{3}$, also producing a low angular contrast with a slight preferential decay in the direction orthogonal to the driving field.

The fact that the radiation pattern of a real atom is more isotropic than the one of a linear dipole questions the idea of having any significant alignment dependent effect. The spontaneous decay of an atom to particular ground states does not depend on the atomic dipole coherence induced by the excitation, but it depends only on the branching ratio of the decay of the excited state (proportional to the square of the Clebsch-Gordan coefficients). This is an outstanding puzzle: Our measurements are in good agreement with a radiating

linear dipole and in disagreement with the radiation expected for the actual multilevel atom. We note that the problem of the radiation of multilevel atoms with degenerate ground states near systems with a modified environment has not been thoroughly addressed or experimentally studied.

IX. DISCUSSION

The numerical calculations have only the ONF radius and the atomic cloud temperature as adjustable parameters to match the experimental results, the former one showing a stronger effect in the expected decay rate. The fact that the decay time of an atomic dipole oriented along the fiber is strongly dependent on the nanofiber radius gives us a possible method to measure this radius. From the error bars in the collected data, and considering the dependence on the nanofiber radius of the simulations, we determine the radius to be 235 ± 5 nm, based on the two-level atom FDTD calculation. This value is close to the estimated ONF radius from the fabrication (240 nm $\pm$ 20). Having fixed the nanofiber radius, there are no free parameters in the calculation of $\langle\gamma\rangle_v/\gamma_0$ (red dotted line in Fig. 6) other than the MOT temperature, set to be 150 μK.

When we calculate the spatial average, as is explained in Sec. VI, we make a series of approximations. These include the van der Waals and Casimir-Polder coefficients calculated for a dielectric plane instead of a cylinder in Eq. (3), an equilibrium distribution of the atomic density in Eq. (4), and the asymptotic expansion of the guided mode for determining the shape of $\alpha(r)$ in Eq. (6). However, when we vary all these quantities (C_3, C_4, ρ, and α) by 20% of their values, the final averaged decay rate does not change by more than the estimated error bars of the measurements.

We can use the physical model presented in this paper to design other experiments. From Figs. 4(a)–4(c) we can see that by positioning the atoms, for example at 50 nm from a 230-nm radius ONF, we can create atomic states that can go from an approximately 40% enhancement of the spontaneous emission to 20% inhibition. This is possible by using only the atomic dipole alignment as a tuning knob for its coupling to the mode of the nanofiber and the environment. We can also use ONFs that support higher-order modes to allow us to have a better control of the probe polarization, using the evanescent field of guided light, which can be used to drive different atomic dipole orientations, such as purely radial or azimuthal.

The discrepancy between different calculations has yet to be understood. It is also necessary to develop a better physical picture that explains the measured behavior for a real multilevel atom near an ONF. This problem brings fundamental questions that need to be revised and systematically studied in the future, crucial for any future application of multilevel atoms coupled to optical waveguides.

X. CONCLUSION

We have experimentally observed the modification of the rate of spontaneous emission of atoms near an optical nanofiber and its dependence on the atomic dipole alignment. The experiment is implemented by placing an ONF at the center of a cold, dilute, atomic cloud. A linearly polarized resonant probe pulse drives the atomic dipoles in a particular alignment. We measured the time distribution of spontaneously emitted photons into the ONF to obtain the atomic lifetime. The modification of the atomic lifetime is measured for different probe polarizations in order to show the dependence on the atomic dipole alignment of the spontaneous emission rate.

A physical model of the experiment is also presented and used to perform a numerical calculation of the modification of the spontaneous emission rate. This shows a good quantitative agreement with the experimental measurements considering two-level atoms. Some basic physical aspects remain elusive, regarding the multilevel structure of a real atom. Theoretical calculations considering the multilevel atom disagree with the experimental observations. We observe a better agreement between the experimental results and the theory for two-level atoms rather than considering multilevel ones, although we have no physical argument to believe that atoms should behave as a two-level system or classical dipoles.

This work clearly demonstrates that there are open problems that need further investigation, a perhaps surprising conclusion given the fundamental nature of the simple problem of an atom radiating near a dielectric. A better understanding of the problem will allow us to extend this knowledge to more general cases. With this knowledge of how atomic properties change under different conditions, we can start implementing a toolbox for precisely manipulating and controlling atoms coupled to optical waveguides.

ACKNOWLEDGMENTS

We would like to thank H. J. Charmichael and A. Asenjo-Garcia for their valuable contributions to the discussion. This research was supported by the National Science Foundation of the United States (NSF) (Grant No. PHY-1307416); NSF (Grant No. CBET-1335857); NSF (Grant No. PHY-1430094); and the USDOC, NIST, Joint Quantum Institute (Grant No. 70NANB16H168). P.B.B. acknowledges the support of PASPA-DGAPA, UNAM, Mexico.

[1] J. D. Thompson, T. G. Tiecke, N. P. de Leon, J. Feist, A. V. Akimov, M. Gullans, A. S. Zibrov, V. Vuletić, and M. D. Lukin, Science **340**, 1202 (2013).

[2] J. Petersen, J. Volz, and A. Rauschenbeutel, Science **346**, 67 (2014).

[3] R. Mitsch, C. Sayrin, B. Albrecht, P. Schneeweiss, and A. Rauschenbeutel, Nat. Commun. **5**, 5713 (2014).

[4] A. Goban, C.-L. Hung, J. D. Hood, S.-P. Yu, J. A. Muniz, O. Painter, and H. J. Kimble, Phys. Rev. Lett. **115**, 063601 (2015).

[5] A. Goban, C.-L. Hung, S.-P. Yu, J. D. Hood, J. A. Muniz, J. H. Lee, M. J. Martin, A. C. McClung, K. S. Choi, D. E. Chang, O. Painter, and H. J. Kimble, Nat. Commun. **5**, 3808 (2014).

[6] R. Yalla, F. Le Kien, M. Morinaga, and K. Hakuta, Phys. Rev. Lett. **109**, 063602 (2012).

[7] J. D. Hood, A. Goban, A. Asenjo-Garcia, M. Lu, S.-P. Yu, D. E. Chang, and H. J. Kimble, Proc. Natl. Acad. Sci. USA **113**, 10507 (2016).

[8] C. Junge, D. O'Shea, J. Volz, and A. Rauschenbeutel, Phys. Rev. Lett. **110**, 213604 (2013).

[9] J. Volz, M. Scheucher, C. Junge, and A. Rauschenbeutel, Nat. Photonics **8**, 965 (2014).

[10] R. N. Patel, T. Schröder, N. Wan, L. Li, S. L. Mouradian, E. H. Chen, and D. R. Englund, Light: Sci. Applicat. **5**, e16032 (2016).

[11] S. Rosenblum, O. Bechler, I. Shomroni, Y. Lovsky, G. Guendelman, and B. Dayan, Nat. Photonics **10**, 19 (2016).

[12] P. Solano, P. Barberis-Blostein, F. K. Fatemi, L. A. Orozco, and S. L. Rolston, Nat. Commun. **8**, 1857 (2017).

[13] D. O'Shea, C. Junge, J. Volz, and A. Rauschenbeutel, Phys. Rev. Lett. **111**, 193601 (2013).

[14] I. Shomroni, S. Rosenblum, Y. Lovsky, O. Bechler, G. Guendelman, and B. Dayan, Science **345**, 903 (2014).

[15] T. G. Tiecke, J. D. Thompson, N. P. de Leon, L. R. Liu, V. Vuletić, and M. D. Lukin, Nature (London) **508**, 241 (2014).

[16] C. Sayrin, C. Junge, R. Mitsch, B. Albrecht, D. O'Shea, P. Schneeweiss, J. Volz, and A. Rauschenbeutel, Phys. Rev. X **5**, 041036 (2015).

[17] Y. Shen, M. Bradford, and J.-T. Shen, Phys. Rev. Lett. **107**, 173902 (2011).

[18] D. E. Chang, A. S. Sørensen, E. A. Demler, and M. D. Lukin, Nat. Phys. **3**, 807 (2007).

[19] B. Gouraud, D. Maxein, A. Nicolas, O. Morin, and J. Laurat, Phys. Rev. Lett. **114**, 180503 (2015).

[20] C. Sayrin, C. Clausen, B. Albrecht, P. Schneeweiss, and A. Rauschenbeutel, Optica **2**, 353 (2015).

[21] D. E. Jones, J. D. Franson, and T. B. Pittman, Phys. Rev. A **92**, 043806 (2015).

[22] R. Kumar, V. Gokhroo, and S. Nic Chormaic, New J. Phys. **17**, 123012 (2015).

[23] E. Fermi, Rev. Mod. Phys. **4**, 87 (1932).

[24] E. M. Purcell, Phys. Rev. **69**, 681 (1946).

[25] P. Milonni, *The Quantum Vacuum* (Academic, New York, 1994).

[26] F. Le Kien and A. Rauschenbeutel, Phys. Rev. A **93**, 043828 (2016).

[27] V. Bordo, J. Opt. Soc. Am. B **29**, 1799 (2012).

[28] J. Barthes, G. Colas des Francs, A. Bouhelier, J.-C. Weeber, and A. Dereux, Phys. Rev. B **84**, 073403 (2011).

[29] P. Lodahl, A. Floris van Driel, I. S. Nikolaev, A. Irman, K. Overgaag, D. Vanmaekelbergh, and W. L. Vos, Nature (London) **430**, 654 (2004).

[30] D. Englund, D. Fattal, E. Waks, G. Solomon, B. Zhang, T. Nakaoka, Y. Arakawa, Y. Yamamoto, and J. Vučković, Phys. Rev. Lett. **95**, 013904 (2005).

[31] P. Lodahl, S. Mahmoodian, and S. Stobbe, Rev. Mod. Phys. **87**, 347 (2015).

[32] B. le Feber, N. Rotenberg, and L. Kuipers, Nat. Commun. **6**, 6695 (2015).

[33] A. T. Nguyen and T. H. Dung, Eur. Phys. J. D **46**, 173 (2008).

[34] H. Nha and W. Jhe, J. Korean Phys. Soc. **32**, 342 (1998).

[35] C. Creatore, L. C. Andreani, M. Miritello, R. Lo Savio, and F. Priolo, Appl. Phys. Lett. **94**, 103112 (2009).

[36] M. S. Eggleston, K. Messer, L. Zhang, E. Yablonovitch, and M. C. Wu, Proc. Natl. Acad. Sci. USA **112**, 1704 (2015).

[37] E. Yablonovitch, Phys. Rev. Lett. **58**, 2059 (1987).

[38] C. Ropp, Z. Cummins, S. Nah, J. T. Fourkas, B. Shapiro, and E. Waks, Nat. Commun. **6**, 6558 (2015).

[39] P. Solano, J. A. Grover, J. E. Hoffman, S. Ravets, F. K. Fatemi, L. A. Orozco, and S. L. Rolston, in *Advances In Atomic, Molecular, and Optical Physics*, edited by E. Arimondo, C. C. Lin, and S. F. Yelin (Academic, New York, 2017), Vol. 66, pp. 439–505.

[40] M. J. Morrissey, K. Deasy, M. Frawley, R. Kumar, E. Prel, L. Russell, V. G. Truong, and S. Nic Chormaic, Sensors **13**, 10449 (2013).

[41] G. Y. Chen, Open Opt. J. **7**, 32 (2013).

[42] J. E. Hoffman, S. Ravets, J. A. Grover, P. Solano, P. R. Kordell, J. D. Wong-Campos, L. A. Orozco, and S. L. Rolston, AIP Advances **4**, 067124 (2014).

[43] F. L. Kien, J. Liang, K. Hakuta, and V. Balykin, Opt. Commun. **242**, 445 (2004).

[44] X. Qi, B. Q. Baragiola, P. S. Jessen, and I. H. Deutsch, Phys. Rev. A **93**, 023817 (2016).

[45] K. Nayak, M. Das, F. L. Kien, and K. Hakuta, Opt. Commun. **285**, 4698 (2012), Special Issue: Optical micro/nanofibers: Challenges and Opportunities.

[46] J. A. Grover, P. Solano, L. A. Orozco, and S. L. Rolston, Phys. Rev. A **92**, 013850 (2015).

[47] M. J. Morrissey, K. Deasy, Y. Wu, S. Chakrabarti, and S. Nic Chormaic, Rev. Sci. Instrum. **80**, 053102 (2009).

[48] E. Vetsch, D. Reitz, G. Sagué, R. Schmidt, S. T. Dawkins, and A. Rauschenbeutel, Phys. Rev. Lett. **104**, 203603 (2010).

[49] D. Reitz, C. Sayrin, R. Mitsch, P. Schneeweiss, and A. Rauschenbeutel, Phys. Rev. Lett. **110**, 243603 (2013).

[50] S. Kato and T. Aoki, Phys. Rev. Lett. **115**, 093603 (2015).

[51] A. Goban, K. S. Choi, D. J. Alton, D. Ding, C. Lacroûte, M. Pototschnig, T. Thiele, N. P. Stern, and H. J. Kimble, Phys. Rev. Lett. **109**, 033603 (2012).

[52] J.-B. Béguin, E. M. Bookjans, S. L. Christensen, H. L. Sørensen, J. H. Müller, E. S. Polzik, and J. Appel, Phys. Rev. Lett. **113**, 263603 (2014).

[53] P. Solano, F. K. Fatemi, L. A. Orozco, and S. L. Rolston, Opt. Lett. **42**, 2283 (2017).

[54] N. V. Corzo, B. Gouraud, A. Chandra, A. Goban, A. S. Sheremet, D. V. Kupriyanov, and J. Laurat, Phys. Rev. Lett. **117**, 133603 (2016).

[55] H. L. Sørensen, J.-B. Béguin, K. W. Kluge, I. Iakoupov, A. S. Sørensen, J. H. Müller, E. S. Polzik, and J. Appel, Phys. Rev. Lett. **117**, 133604 (2016).

[56] P. Lodahl, S. Mahmoodian, S. Stobbe, P. Schneeweiss, J. Volz, A. Rauschenbeutel, H. Pichler, and P. Zoller, Nature (London) **541**, 473 (2017).

[57] V. V. Klimov and M. Ducloy, Phys. Rev. A **69**, 013812 (2004).

[58] F. Le Kien, S. Dutta Gupta, V. I. Balykin, and K. Hakuta, Phys. Rev. A **72**, 032509 (2005).

[59] F. Le Kien and A. Rauschenbeutel, Phys. Rev. A **90**, 023805 (2014).

[60] F. Le Kien, V. I. Balykin, and K. Hakuta, Phys. Rev. A **73**, 013819 (2006).

[61] F. L. Kien and K. Hakuta, Phys. Rev. A **77**, 013801 (2008).

[62] F. Le Kien and K. Hakuta, Phys. Rev. A **78**, 063803 (2008).

[63] K. Hakuta and K. P. Nayak, Adv. Nat. Sci.: Nanosci. Nanotechnol. **3**, 015005 (2012).

[64] M. Almokhtar, M. Fujiwara, H. Takashima, and S. Takeuchi, Opt. Express **22**, 20045 (2014).

[65] N. R. Verhart, G. Lepert, A. L. Billing, J. Hwang, and E. A. Hinds, Opt. Express **22**, 19633 (2014).
[66] M. Gaio, M. Moffa, M. Castro-Lopez, D. Pisignano, A. Camposeo, and R. Sapienza, ACS Nano **10**, 6125 (2016).
[67] E. Fermi, *Nuclear Physics* (The University of Chicago Press, Chicago, 1949).
[68] E. A. Hinds, in *Advances In Atomic, Molecular, and Optical Physics*, edited by D. Bates and B. Bederson (Academic, New York, 1990), Vol. 28, pp. 237–289.
[69] A. Corney, *Atomic and Laser Spectroscopy* (Oxford University Press, Oxford, 1979).
[70] C. W. Oates, K. R. Vogel, and J. L. Hall, Phys. Rev. Lett. **76**, 2866 (1996).
[71] D. O'Connor and D. Phillips, *Time-Correlated Single Photon Counting* (Academic, New York, 1984).
[72] F. K. Fatemi, J. E. Hoffman, P. Solano, E. F. Fenton, G. Beadie, S. L. Rolston, and L. A. Orozco, Optica **4**, 157 (2017).
[73] Any mention of commercial products in a publication having NIST authors is for information only; it does not imply recommendation or endorsement by NIST.
[74] B. D. Patterson, P. Solano, P. S. Julienne, L. A. Orozco, and S. L. Rolston, Phys. Rev. A **97**, 032509 (2018).
[75] A. F. Molisch and B. P. Oehry, *Radiation Trapping in Atomic Vapours* (Oxford University Press, Oxford, 1998).
[76] J. E. Simsarian, L. A. Orozco, G. D. Sprouse, and W. Z. Zhao, Phys. Rev. A **57**, 2448 (1998).
[77] U. Volz and H. Schmoranzer, Phys. Scr. **1996**, 48 (1996).
[78] P. R. Bevington and D. K. Robinson, *Data Reduction and Error Analysis for Physical Sciences* (McGraw-Hill, New York, 2003).
[79] L. Novotny and B. Hecht, *Principles of Nano-Optics* (Cambridge University Press, Cambridge, 2012).
[80] H. Tanji-Suzuki, I. D. Leroux, M. H. Schleier-Smith, M. Cetina, A. T. Grier, J. Simon, and V. Vuletić, Adv. At. Mol. Opt. Phys. **60**, 201 (2011).
[81] A. Taflove and S. C. Hagness, *Computational Electrodynamics: The Finite-Difference Time-Domain Method*, 3rd ed. (Artech House, Boston, 2005).
[82] A. Asenjo-Garcia, J. D. Hood, D. E. Chang, and H. J. Kimble, Phys. Rev. A **95**, 033818 (2017).
[83] A. Asenjo-Garcia, M. Moreno-Cardoner, A. Albrecht, H. J. Kimble, and D. E. Chang, Phys. Rev. X **7**, 031024 (2017).
[84] F. L. Kien and K. Hakuta, Phys. Rev. A **77**, 042903 (2008).
[85] L. Russell, D. A. Gleeson, V. G. Minogin, and S. Nic Chormaic, J. Phys. B: At., Mol. Opt. Phys. **42**, 185006 (2009).
[86] J. A. Grover, Atom-trapping and photon-counting experiments with optical nanofibers, Ph.D. thesis, University of Maryland, 2015.
[87] G. Sagué, E. Vetsch, W. Alt, D. Meschede, and A. Rauschenbeutel, Phys. Rev. Lett. **99**, 163602 (2007).
[88] Q. Quan, I. Bulu, and M. Lončar, Phys. Rev. A **80**, 011810 (2009).
[89] D. Polder and M. F. H. Schuurmans, Phys. Rev. A **14**, 1468 (1976).